Adaptive Cross-Correlation Algorithm and Experiment of Extended Scene Shack-Hartmann Wavefront Sensing

Erkin Sidick*, Rhonda M. Morgan, Joseph J. Green, Catherine M. Ohara, and David C. Redding
Jet Propulsion Laboratory, California Institute of Technology, 4800 Oak Grove Drive, Pasadena, CA, USA 91109

ABSTRACT

We have developed a new, adaptive cross-correlation (ACC) algorithm to estimate with high accuracy the shift as large as several pixels in two extended-scene images captured by a Shack-Hartmann wavefront sensor (SH-WFS). It determines the positions of all of the extended-scene image cells relative to a reference cell using an FFT-based iterative image-shifting algorithm. It works with both point-source spot images as well as extended scene images. We have also set up a testbed for extended-scene SH-WFS, and tested the ACC algorithm with the measured data of both point-source and extended-scene images. In this paper we describe our algorithm and present our experimental results.

Keywords: Adaptive optics, Shack-Hartmann sensor, extended scene, remote imaging, wave-front sensing and control

1. INTRODUCTION

A Shack-Hartmann wavefront sensor (SH-WFS) consists of a lenslet array located in a plane conjugate to a wavefront error source and a camera located in the focal plane of the lenslet array. Its simplicity, inexpensiveness and real-time data processing capability has made the SH sensor a popular wavefront sensing instrument in various areas including astronomical adaptive optics, optical testing and ocular aberrometry since its invention [1]. The conventional method used in an SH-WFS first produces a grid of spot images from a point-source, then retrieves the phase information from the estimates of the offsets between these spot image positions and a set of pre-determined reference positions. When used in a closed-loop wavefront sensing and control system of a telescope, it offers high dynamic range, albeit with a lower wavefront measurement resolution than, for example, the Modified Gerchberg-Saxton (MGS) WFS approach [2]. In some applications of space-based, airborne, and ground-based adaptive optical systems, extended-scene SH-WFS provides some great benefits. In an extended-scene SH-WFS, the lenslet array produces sub-images at the SH camera, and wavefront phase error shifts these sub-images from their original positions. Therefore, in order to measure wavefront error, one needs to estimate the shifts of these sub-images from their ideal positions. Recently, Poyneer reported a periodic correlation technique to obtain an estimate on the sub-pixel shift between two scene-based images [3]. In that approach, the periodic correlation of a sub-image with a specific reference sub-image is taken, then the shift is estimated by parabolic sub-pixel interpolation of the correlation peak location. It was confirmed experimentally that for point-source based adaptive-optics (AO) system, the periodic correlation technique is more accurate, more robust to changing conditions and provides lower noise than a centroiding algorithm [4-5].

We have developed a new, adaptive cross-correlation (ACC) algorithm to estimate with high accuracy the shift as large as several pixels between two extended-scene images captured by an SH-WFS. It determines the positions of all of the extended-scene image cells relative to a reference cell using an FFT-based iterative image-shifting algorithm. We have developed some preliminary failsafe criteria for both point-source and extended-scene images to be processed. Based on those criteria, the corresponding code of the ACC algorithm first determines if an SH image is from a point source or an extended scene, then it applies different failsafe criteria to determine if an SH image is acceptable or not for wavefront sensing. This made it possible for the ACC code to work autonomously on an SH image. We tested the shift estimation accuracy of the ACC algorithm with both point-source and extended-scene images. We also compared its phase estimation accuracy with that of a conventional centroid-finding algorithm, and obtained good agreement between the two approaches. Our investigation conducted with the ACC algorithm has re-confirmed some of the above-mentioned advantages of the periodic correlation technique over the conventional centroiding algorithm. In this paper we describe our algorithm and present some experimental results.

---

*Erkin.Sidick@jpl.nasa.gov; Phone 1 818 393-7585; Fax 1 818 393-9471; www.jpl.nasa.gov

2. BRIEF DESCRIPTION OF THE ACC ALGORITHM

The ACC algorithm has been reported in detail elsewhere [6-7]. Therefore, we review it only briefly here. An extended-scene SH-WFS images a scene, not a point source as in the conventional case. An example of such a scene is given in **Fig. 1(a)**. The lenslet array in the SH-WFS creates a grid of sub-images at the SH camera as shown in **Fig. 1(b)**, and each of these sub-images looks like the example shown in **Fig. 1(c)**. This 64x64 pixel sub-image becomes much blurred as compared to the original scene, because its diffraction limit is defined by each lenslet array sub-aperture, not the whole aperture of the optical system.

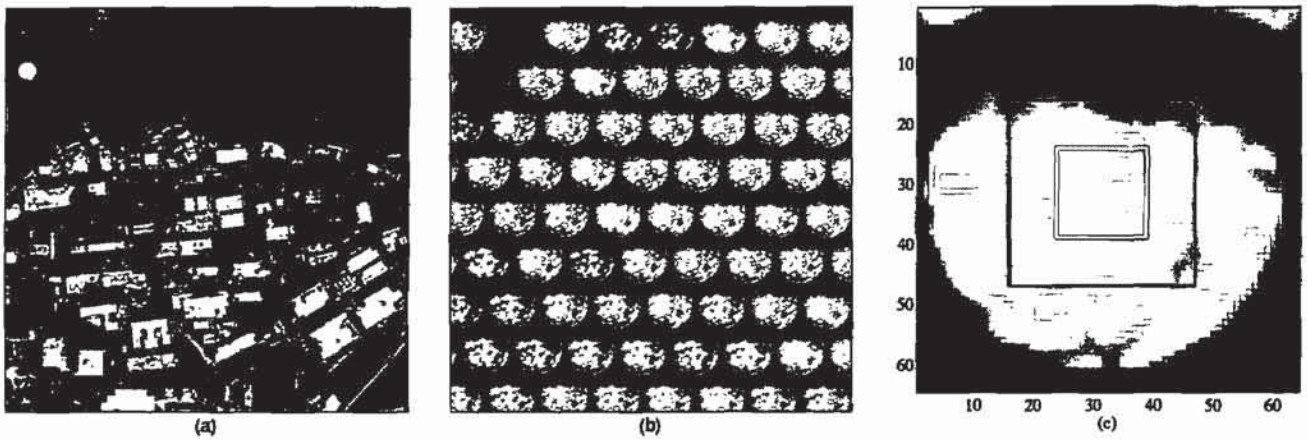

Figure 1. (a) An example of extended scenes to be imaged by an extended-sceneSH sensor. (b) Part of an extended scene image captured by a SH camera. It was obtained by convolving the image shown in part (a) with a measured SH point-source spot image. (c) One 64x64 pixel sub-image obtained from the SH image shown in part (b).

The ACC algorithm is based on the following property of Fourier-transform: Position shift in the image domain corresponds to a linear phase in the Fourier-domain. That is,

$$\begin{aligned} & s(x, y) \leftrightarrow \hat{s}(u, v) \\ & s(x-\Delta x, y-\Delta y) \leftrightarrow \hat{s}(u, v) \mathrm{e}^{-j 2 \pi(\Delta x u+\Delta y v)} \end{aligned}, \tag{1}$$

where $s(x,y)$ is a sub-image or cell as highlighted by a white frame in Fig. 1(c), $\hat{s}(u,v)$ is its Fourier-transform, and the $\leftrightarrow$ symbol represents the forward and the inverse Fourier-transform operations. If we take a test cell $s(x,y)$ and a reference cell $r(x,y)$, then, under an ideal condition, the test cell is just a copy of the reference cell only shifted in position by $\{\Delta x,\Delta y\}$, that is, $s(x,y)=r(x-\Delta x,y-\Delta y)$. In such a case, if we construct a cross-correlation function, $\hat{c}(u,v)$, of the test and the reference cells in the Fourier-domain, that is,

$$\hat{c}(u, v) \leftrightarrow r^{*}(u, v) \hat{s}(u, v)=\left|\hat{c}(u, v)\right| \mathrm{e}^{-j \varphi(u, v)}, \tag{2}$$

then its phase becomes a linear function of $\{u,v\}$. That is, $\varphi(u,v)=2\pi(\Delta x u+\Delta y v)$, and the $\{\Delta x,\Delta y\}$ correspond to the shift of the test cell relative to the reference cell along the x-axis and the y-axis, respectively. The "*" symbol in Eqn. (2) indicates a complex conjugate.

In the real world, however, the test cell is not only a shifted version of the reference cell, its texture or content can also be different from that of the reference cell. In such a case, the $\varphi(u,v)$ becomes a non-linear function of $\{u,v\}$ and the coefficients of its linear components in the u-axis and v-axis directions contain $\{\Delta x,\Delta y\}$. Therefore, the problem of finding the shift of a test cell relative to the reference cell reduces to the problem of finding the linear phase coefficients or u- and v-slopes of $\varphi(u,v)$.

The computer code of the ACC algorithm finds $\{\Delta x,\Delta y\}$ adaptively through a *while-loop* in the following way: It finds $\{\delta x,\delta y\}$ in the current slope-finding iteration. Then it accumulates $\{\delta x,\delta y\}$ in the form of $\Delta x=\Delta x+\delta x$ and $\Delta y=\Delta y+\delta y$, respectively, and also calculates the test cell shift, Δs, found in the present iteration, $\Delta s=\sqrt{\delta x^2+\delta y^2}$. If this Δs is greater than a pre-set tolerance or the total number of iterations is still smaller than a pre-set limit, then the code shifts the test cell with a larger dimension, $S(x,y)$ as shown with a black frame in Fig. 1(a), by $\{-\Delta x,-\Delta y\}$ via an inverse Fourier-transform operation,

$$S(x+\Delta x, y+\Delta y) \leftrightarrow \hat{S}(u,v)\mathrm{e}^{j2\pi(\Delta xu+\Delta yv)} \quad , \tag{3}$$

and repeats the slope-finding iteration one more time. Otherwise it terminates the *while-loop*. Because the slope-finding operation is carried out in such an iterative way, very high accuracy, such as that better than 0.01 pixel, can be achieved with this algorithm. In our present case, the $s(x,y)$ and the $r(x,y)$ have a size of 16x16 pixel, and the $S(x,y)$ has a size of 32x32 pixel. Using such smaller cells $s(x,y)$ and $r(x,y)$ in the slope-finding process makes the data-processing faster and also increases the dynamic range of the SH-WFS. Whereas using a larger cell $S(x, y)$ for image-shifting prevents the shifted test cell $s(x,y)$ from wrap-around error.

The shift-finding steps described above are for finding the shift of one test cell relative to the reference only. In order to find the shifts of all of the cells in an SH camera image, one only needs to repeat the above steps for N times, where N is the total number of cells. For each SH camera image, one cell is chosen as a reference cell, ideally from the approximate center of the whole image, and the remaining cells become the test cells.

3. TESTBED

A picture and a schematic diagram of the SH-WFS testbed at JPL are shown in **Figs. 2(a) and 2(b)**, respectively. The testbed employs a deformable mirror (DM) to introduce a known aberration that is measured by both a SH camera and a Phase Retrieval Camera (PRC). The main component of the testbed is a field projector consisting of three identical off-

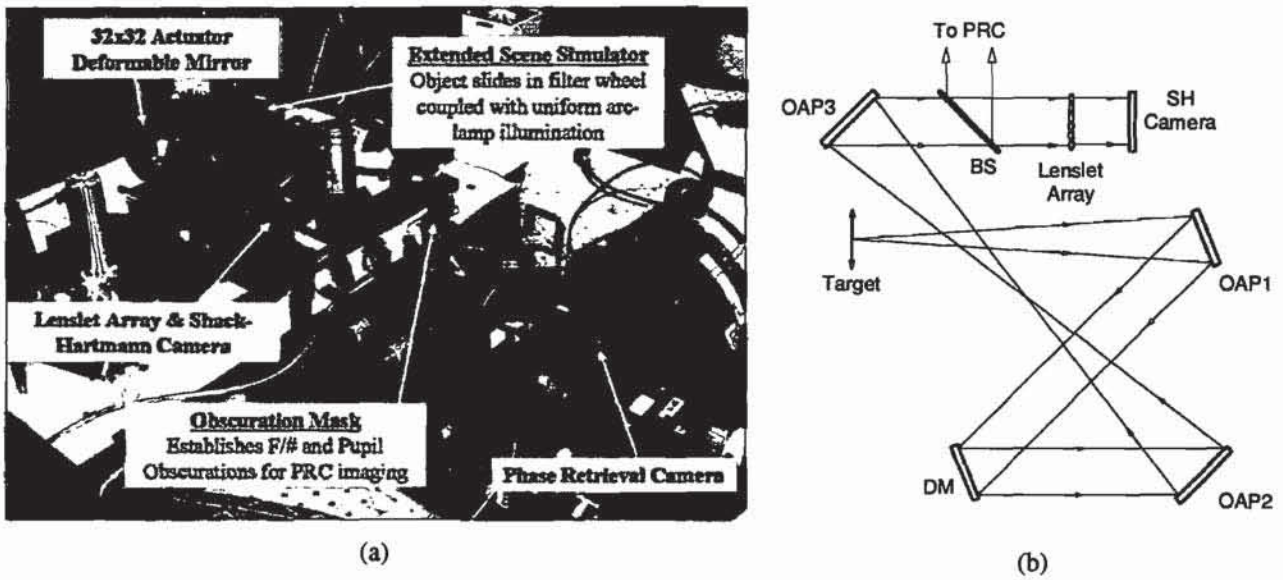

Figure 2. (a) A photograph and (b) the corresponding schematic diagram of the SH-WFS testbed at JPL.

axis parabolas, OAP1 though OAP3, as shown in Fig. 2(b). It provides a pupil to both the SH camera and the PRC that is conjugate to the DM. The source is a mercury-zenon arclamp delivered through a liquid light guide, and imaged through a diffuser onto the target. It can be used with a pinhole located in a filter wheel to provide a point source as well. The filter wheel also holds other targets, including a bar target made of a chrome pattern deposited on a glass. The

target is located at the focus of OAP1. This OAP collimates the light beam. The collimated beam is incident on the DM first, then it is re-imaged through two matched OAPs, OAP2 and OAP3, to the exit pupil. A beam-splitter directs one beam to the entrance pupil of the PRC and allows the main beam to continue to the SH lenslet array.

The lenslet array has a pitch of 300μm and f/25.3, and the SH camera has square pixels with a width of 5μm. This results in approximately 8 pixels per Airy disc diameter at a wavelength of 650nm. The DM has 1024 (32x32) actuators arrayed on a 1mm pitch, and one pitch spacing corresponds to about 3.5 sub-apertures. More information about this testbed can be found in **Ref. [8]**.

4. RESULTS

We now present some results on the tests conducted on the ACC algorithm as well as those of wavefront sensing and control experiments.

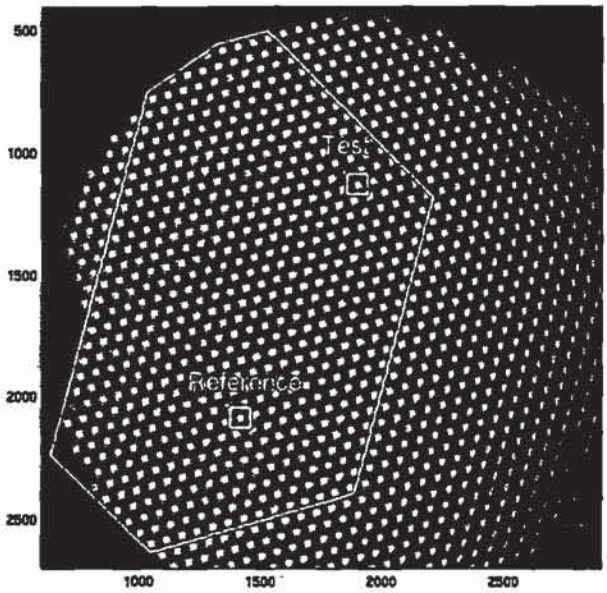

Figure 3. An SH camera image taken on the SH-WFS testbed at JPL. The window inside the white frame is one of the active windows of the SH camera to be used in this study. The Reference and the Test cells indicated on this figure are the ones chosen to test the ACC algorithm. The gray-level of the SH camera is 0 – 4095.

4.1 Accuracy and Speed of the ACC Algorithm

Figure 3 shows an extended scene image taken with the SH camera on our testbed by using the bar target. The field projector in our testbed was originally designed for a smaller field of view (FOV), but we had to use it with a larger FOV to match it with the rest of testbed hardware. Therefore, it introduced some vignetting to the system's clear aperture. Obtaining a field projector matched to our testbed was not possible because of some funding and schedule constraints. Therefore, we chose a portion of the whole image outlined by the white frame in Fig. 3 to test the ACC algorithm (We sometimes used a window slightly larger than this white-frame window). The sub-images inside this window suffer less from vignetting as compared to the other part of the image. There are 78 actuators inside this window, and we chose about 450 image cells to analyze.

In order to test the accuracy and the speed of the ACC algorithm, we took 8 SH camera images, each with a different integration time. From each image, we chose one reference and one test cells, as shown in Fig. 3, where the two cells are about 16 sub-image apart from each other. This guaranteed that not only the relative locations of these two cells are different, so are their contents also. The different integration times produced images with different image qualities, as shown in **Fig. 4**. These are the 32x32 pixel test cells corresponding to 8 different integration times. Given in the figure title of each part is the integration time in ms, and that in the x-label are the gray-level (minimum – maximum) and the total number of saturated pixels inside the smaller (indicated by a red frame), 16x16 pixel cell. The SH camera in our

testbed had vertical gain non-uniformity which caused some artificial vertical lines in the captured image. Such vertical lines are clearly visible in Fig. 4. As we can see, in the last part of Fig. 4 (Time = 39.7ms), 77 pixels inside the 16x16 pixel cell are saturated.

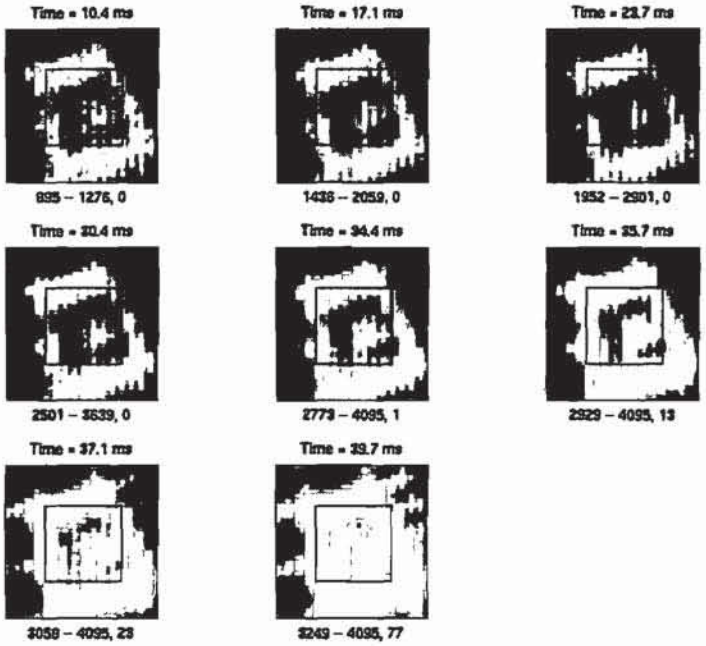

Figure 4. 32x32 pixel test cells corresponding to 8 different integration time values. The red frame indicates a smaller, 16x16 pixel cell. The integration time value is shown as the figure title in each part, and x-label shows the gray-level range (minimum – maximum) and the total number of saturated pixel in the corresponding 16x16 pixel cell having a total of 256 pixels.

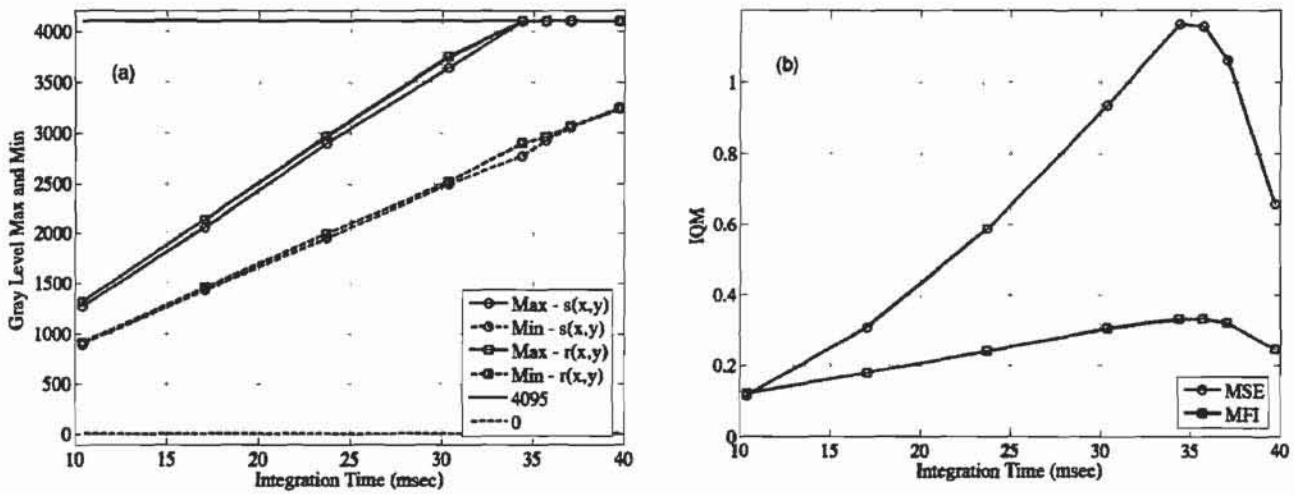

Figure 5. (a) Maximum and minimum luminance values of the test cell and the reference cell signals captured by the SH camera having a gray-level of 0 – 4095 versus the integration time. (b) Average MSE and MFI values of the test cell and the reference cell signals versus integration time.

We examined several image quality metric (IQM) functions in order to establish failsafe criteria in terms of the quality of an extended scene image for the ACC algorithm. . We found that, the averaged mean-squared-error (MSE) and modified Fisher-information (MFI) values of all of the cells in an extended scene image can predict well if the quality of an image is acceptable or not for the analysis with the ACC algorithm. For the *i*th cell, these two IQM functions are given by [9]

$$MSE_i = \sum_{x,y} \left| \Psi_i(x,y) - \overline{\Psi}_i \right|^2$$

$$MFI_i = 4 \times \sum_{x,y} [\nabla a_i(x,y)]^* \bullet \nabla a_i(x,y) \quad , \tag{4}$$

$$\Psi_i(x,y) = S_i(x,y)/4095, \quad a_i(x,y) = \sqrt{\Psi_i(x,y)}$$

where $\overline{\Psi}_i$ is the average value of $\Psi_i(x,y)$. We will discuss the failsafe criteria of the ACC algorithm in a later section of this paper. **Figure 5(a)** shows the extreme luminance values of the 8 pairs 32x32 pixel test and reference cell signals as a function of integration time, and **Fig. 5(b)** shows the corresponding mean values of MSE and MFI. As is seen from Fig. 5(b), the MSE parameter is fairly sensitive to the quality of the extended scene image taken on our testbed, and varies a lot with integration time.

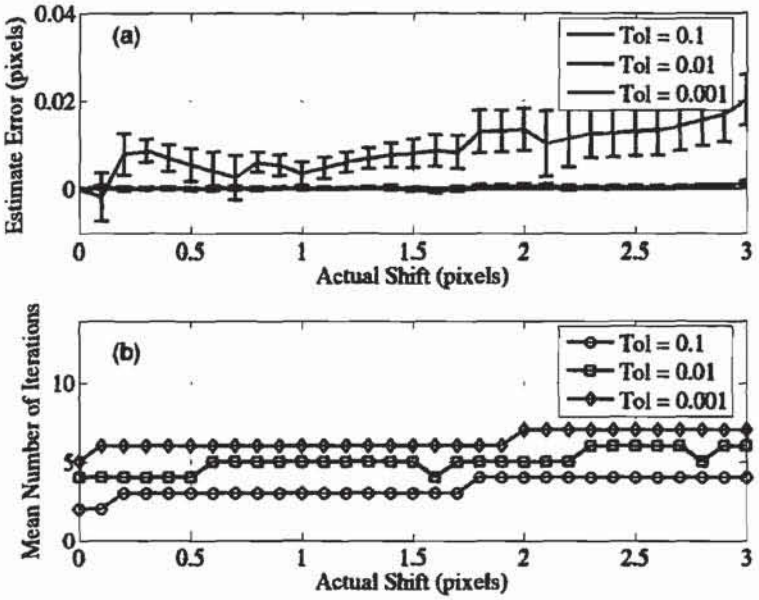

Figure 6. Trade-off between the estimate accuracy and the computation speed. Part (a) shows the estimate error as a function of the actual shift, and part (b) show the mean number of iterations required to obtain the results in part (a). The solid curves and the error barfs in part (a) represent the mean and the standard deviation values of the 8 different data points corresponding to the 8 different integration times. "Tol" in the figure legend is the image-shifting iteration tolerance value.

We tested the shift estimate accuracy and the speed of the ACC algorithm in the following way. We first shifted the test cell along the *y*-axis by a known distance by convolution, then used the ACC algorithm to estimate the shift between this shifted test cell and the original reference cell. Unlike the case reported in **Ref. [7]**, we chose the *y*-axis direction for the actual shift here to find out how much these new results differ from those obtained by shifting the test cell in the *x*-axis direction. The vertical lines in the SH image increase the image contrast in the *x*-axis direction, so one can expect that more iterations are needed in the *y*-axis direction to achieve the same accuracy. We repeated this simulation for all the 8 pairs of cells and for 3 different image-shifting iteration tolerance values. From such simulations we obtained the results shown in **Fig. 6.** Part (a) of this figure shows the estimate error (the shift estimate obtained with the ACC algorithm

minus the actual shift) as a function of actual shift introduced, and part (b) shows the corresponding mean number of iterations required to obtained the results in part (a). The solid curves and the error bars in part (a) represent the mean and the standard deviation values of the estimate error corresponding to the 8 integration times. These results clearly show that only about 5 iterations are required to achieve an estimate accuracy of 0.01 pixel. It was shown previously that to achieve the same accuracy on the same image data for the actual shift in the x-axis direction, approximately 4 iterations on the average are required [7]. That is, even though the content of each cell changes quite differently in the x- and the y-directions, the required shift estimate iteration numbers stay almost the same and they are fairly small. This is one of the most important features of this algorithm. In our case, when using a Linux-based Intel Xeon 3.2Ghz dual-processor workstation, it took approximately 10 seconds for reconstructing the wavefront error from about 450 cells.

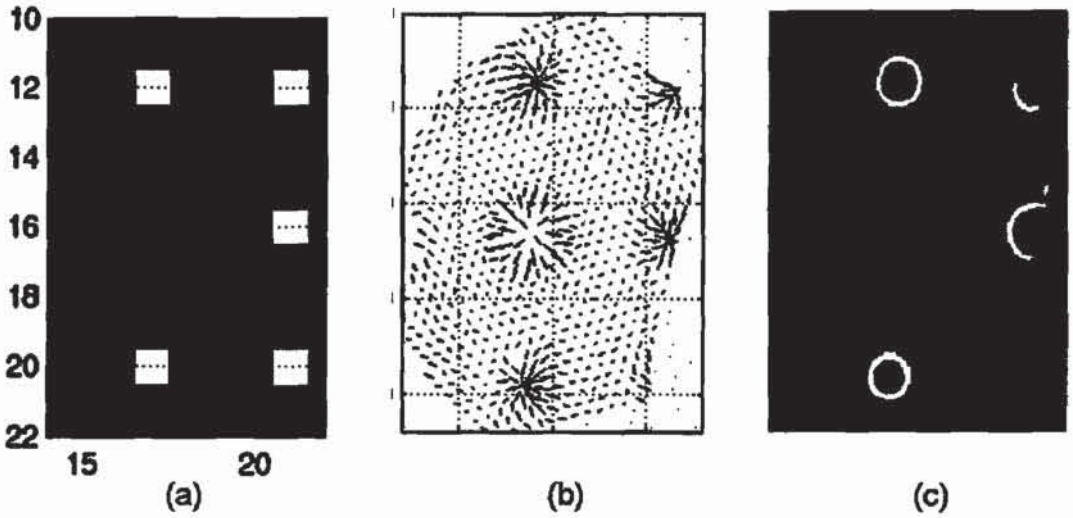

Figure 7. An example of the wavefront sensing results obtained on our testbed by analyzing a point-source image data with the ACC algorithm. (a) Actuator poke pattern applied to the DM. One in every 4 actuators was poked by either 15V (white box) or -15V (black box) voltage. (b) Measured offset diagram. (c) Reconstructed OPD map. The RMS and the PV (peak-to-valley) values of this OPD map are 29.3 and 273.3nm, respectively. The x- and the y-labels in part (a) are the actuator numbers. The size of the active window used in this case is slightly bigger than that shown in Fig. 3.

4.2 Examples of Wavefront Sensing and Control (WFS&C) Using the ACC Algorithm

Figure 7 shows an example of the SH wavefront sensing conducted on our testbed. It was obtained by analyzing a point-source spot image with the ACC algorithm. Part (a) is the actuator poke pattern applied to the DM, part (b) is the measured offset diagram, and part (c) is the reconstructed OPD map. **Figure 8** compares the OPD maps measured from the images of a point source and the bar target, respectively. One actuator in every 3 was poked with 15V voltage in these experiments. The two sets of image data were taken on different days, and there was slight difference in the registration of actuators at the SH camera due to different light sources. These factors caused some difference in the OPD maps, especially at the edges, as is seen from this figure.

The actuator poke pattern shown in Fig. 7(a) is one of the 16 different 4x4 actuator patterns used in our experiments to test the ACC algorithm. In the remaining 15 cases, different groups of actuators were poked in a similar 4x4 actuator pattern. When we tried to compare our ACC algorithm with a centroiding algorithm by processing the 16 data sets taken with a point source on a day different from the date of the data in Fig. 7, the centroiding algorithm failed in 4 cases. The OPD maps of one failed case, Case #15, are shown in **Fig. 9**. They were obtained by analyzing the same image data with both the centroiding and the ACC algorithms, respectively. The image luminance threshold value in our centroiding algorithm was originally to 100, and it produced the OPD map shown in **Fig. 9(a)**. But the ACC algorithm still produced a clean OPD map as shown in **Fig. 9(b)** which corresponds well to the actuator poke pattern and is comparable to the results obtained with the ACC algorithm in other 15 cases. After examining the image data carefully, we found that both the peak and the background luminance values of all the 32x32 pixel cells are much bigger in the failed cases as compared to the other good cases. Also, in those 4 failed cases, some cells had "hot pixels" in the surrounding areas of the spot images. In order to get a better understanding on this issue, we sorted the

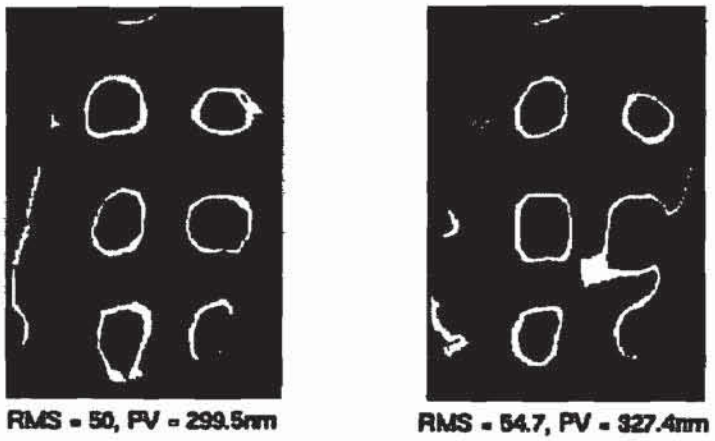

Figure 8. Comparison of the OPD maps measured from the images of (a) a point source and (b) the bar target, respectively. They were obtained by poking one actuator in every 3 with a 15V voltage.

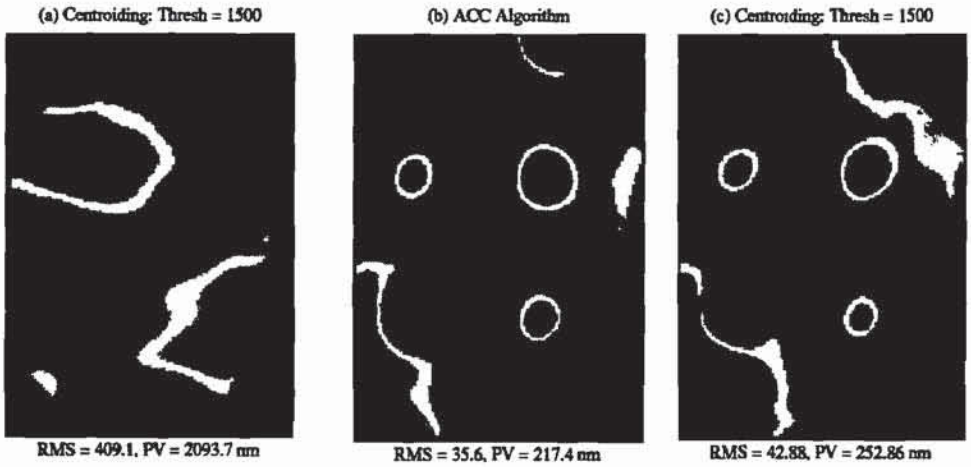

Figure 9. Same as Fig. 7 except a different group of actuators were poked in this experiment. (a) OPD map obtained with a centroiding algorithm. (b) OPD map obtained with the ACC algorithm.

$S_i(x, y)$, and averaged its smallest 20 and the largest 5 pixels, respectively. Then we averaged these two quantities for each case separately to get the "Minimum" and "Maximum" values shown **Fig. 10**. We can see the failed 4 cases, Cases #5 – #7 and #15, very clearly in this figure. This result gave us a new idea: Try to increase the image threshold in the centroiding algorithm. When we increased the threshold from 100 to 1500, we obtained the OPD map shown in **Fig. 9(c)**. It is much better than before, but its RMS value is still 16% larger than the result obtained with the ACC algorithm. These findings prove that the ACC algorithm suffers much less from the background level and the "hot pixel" noise in the image data as compared to the centroiding algorithm. It also proves that the ACC algorithm works well on spot images whose luminance range can vary a lot. We had up to 10 saturated pixels in each $S_i(x, y)$ in some of our measured point source spot images, and the ACC still produced acceptable results. The same was true for extended scene images. In the latter case, the ACC algorithm produced reasonably good results when some 32x32 pixel cells had up to 100 saturated pixels.

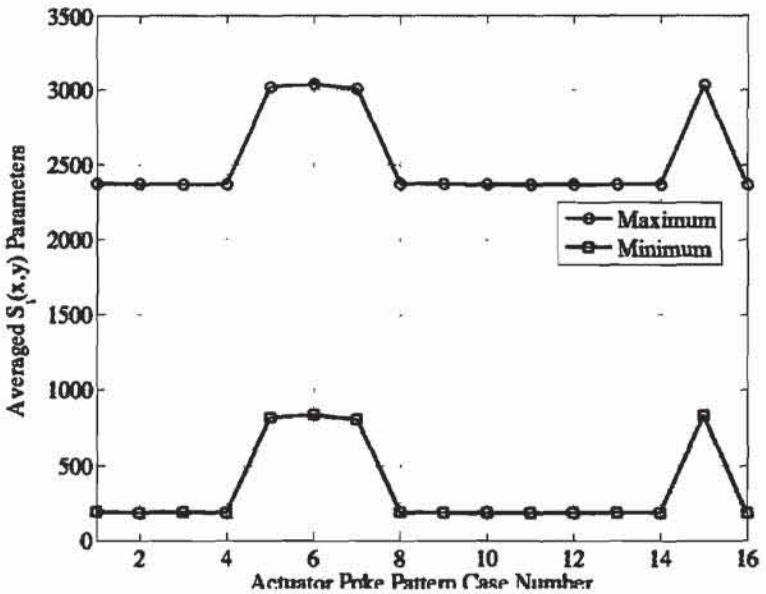

Figure 10. Same as Fig. 7 except a different group of actuators were poked in this experiment. (a) OPD map obtained with a centroiding algorithm. (b) OPD map obtained with the ACC algorithm.

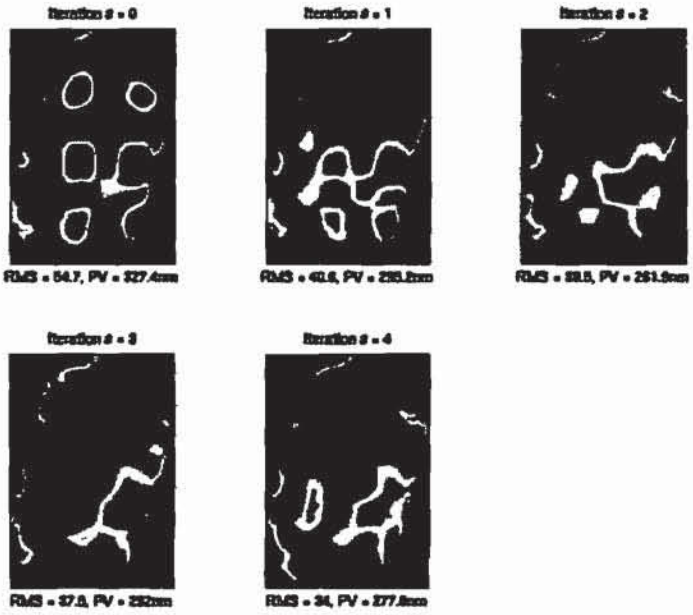

Figure 11. Results of an WFS&C experiment conducted with the bar target. The original actuator poke pattern is the same as in Fig. 8. A total of 4 WFC iterations were carried out retaining only 50 eigen-modes in the gain matrix.

We have also carried out several WFS&C experiments with extended scene bar target. For such experiments, we first measured the influence functions of all 78 actuators inside the active window , then obtained the corresponding singular value decomposition matrices. From that we constructed gain matrices with different number of eigen-modes (non-singular values). **Figure 11** shows the results of one extended scene WFS&C experiment conducted on our testbed by retaining only 50 eigen-modes in the gain matrix. The actuator poke pattern is the same as in the case of Fig. 8, and the OPD map before WFC is given as "Iteration = 0" in this figure. The remaining 4 plots show the reconstructed OPD maps at the end of 4 different WFC iterations. As is seen from this figure, the RMS wafefront error is reduced from the original 54.7 nm to 34.0 nm after 4 WFC iterations. The residual wavefront error that we see in the plot of "Iteration =

4" is probably caused by the most part by the reduced number of eigen-modes, and to a lesser degree by the measurement errors in the extended scene influence functions of the DM. Nevertheless, to our knowledge, this is the first extended scene SH wavefront control experiment that has ever been reported. This preliminary result clearly demonstrates the applicability of the extended scene SH-WFS in the course sensing and control of large wavefront errors in an adaptive optical system.

5. ON THE FAILSAFE CRITERIA OF THE ACC ALGORITHM

We have conducted some preliminary studies on the failsafe criteria of the ACC algorithm, and come up with some check list quantities related to the parameters of the dark and the signal images. In this section, we briefly describe our findings.

Our ACC algorithm code works on a dark and a signal images that are normalized by 4095, which effectively converts the gray-levels of both the dark and the signal images from 0 – 4095 to 0 – 1. It initially checks the signal-to-dark ratio (SDR). To calculate the SDR, the code first calculates the mean luminance values of each 32x32 pixel dark and signal cells individually, and averages them separately for all the dark and the signal cells. The ratio of these two quantities is the SDR. The ACC code then proceeds to the next step if SDR > 1, but rejects the image otherwise.

Next, the code calculates the average MSI and MFI values of the original (without dark subtraction) 32x32 pixel signal image cells, and goes to the following step if these MSE and MFI values are greater than 0.1. Otherwise it rejects the image. Following that the code checks the mean value of the Peak-to-Edge Ratio (P2ER). For each cell, the P2ER is the ratio of the mean of the 5x5 pixel area in the cell centered at the maximum luminance pixel to the mean of the 2-pixel wide edges of the cell excluding those pixels which are part of the 5x5 pixel peak area. For the image data measured in our testbed with different integration times, we found that the overall (or average) P2ER > 1.2 for a point source, and it is very close to 1 for our extended scene bar target. Therefore, we chose P2ER > 1.2 as the criterion for categorizing an image as a point source image. In addition to P2ER, the ACC code also uses the average number of saturated pixels of all the 16x16 pixel cells, NSP, as another acceptance criterion. If the ACC code determined that an image is a point source image, then it accepts the image if P2ER $\geq$ 2 and NSP $\leq$ 3. Otherwise it rejects the image. If an image is an extended scene image, then the ACC code accepts it if NSP < 50 and SDR > 10. These criteria were derived based on many sets of image data measured by using a point source and the extended scene bar target with different integration times. To make them more perfect, it is necessary to try these criteria on different scenes having various contrast levels, as well as by analyzing the different areas of the same image taken on a vignetting-free system.

6. CONCLUSION

We have presented an important advance in extended-scene SH-WFS, the Adaptive Cross-Correlation (ACC) algorithm. It finds the shift between a test and a reference image cells iteratively to any desired accuracy by using an FFT based image-shifting algorithm. It has been shown that under a normal extended scene image condition, the ACC algorithm achieves a shift estimate precision of 0.01 pixel in about 5 image-shifting iterations.

We built an SH-WFS testbed to test our ACC algorithm, and conducted some experiments with both a point source and an extended scene bar target. When processing the same point-source image data of good quality, both of our centroiding and ACC algorithms gave very similar results. In some cases of spot image data, the ACC algorithm produced acceptable results while the centroiding algorithm failed. It was found that those image data had relatively high background noise and contained "hot pixels" in the vicinity of some spot images. We analyzed with the ACC algorithm a point-source spot image and an extended scene image taken by applying the same actuator poke pattern to the DM, and obtained good agreement between the two results. In addition, we have presented the results on one of our extended scene SH wavefront sensing and control experiment as an example.

We also described our preliminary failsafe criteria on the ACC algorithm. They were developed based on the point-source and the extended-scene image data measured on our testbed with different integration times. They were tested to certain extent on our testbed, and gave satisfactory results. These criteria can be more perfected by trying them on different extended scene images and on the different parts of the same extended scene image.

The ACC algorithm presented in this paper extends the application of SH-WFS even further, enabling AO systems to use arbitrary extended scenes in Shack-Hartmann based wavefront sensing instead of a point source.

REFERENCES

1. I. Ghozeil, "Hartmann and other screen tests,", in *Optical Shop Testing 2nd Edition*, D. Malacara, ed., pp. 367-396, Wiley, New York, 1992.
2. Scott A. Basinger, David C. Redding, Andrew E. Lowman, Laura A. Burns, Karen Y. Liu, and David Cohen, "Performance of wavefront sensing and control algorithms on a segmented telescope testbed," *Proc. SPIE* **4013**, 749 (2000).
3. Lisa A. Poyneer, "Scene-based Shack-Hartmann wave-front sensing: analysis and simulation," Appl. Opt. 42, 5807 (2003).
4. Lisa A. Poyneer, Kai La Fortune, and Carri Chan, "Secen-based wave-front sensing for remote imaging," *Proc. SPIE* **5162**, 91 (2003).
5. Lisa A. Poyneer, David W. Palmer, Kai N. LaFortune, and Brian Bauman, "Experimental results for correlation-based wavefront sensing," *Proc. SPIE* **5894**, 58940N-1 (2005).
6. Erkin Sidick, Joseph J. Green, Catherine M. Ohara, and David C. Redding, "An adaptive cross-correlation algorithm for extended scene Shack-Hartmann wavefront sensing," in *Adaptive Optics: Analysis and Methods; Computational Optical Sensing and Imaging; Digital Holography and Theree-Dimenitonal Imaging; and Signal Recovery and Synthesis on CD-ROM* (The Optical Society of America, Washington, DC, 2007), paper JTuA7.
7. Erkin Sidick, Joseph J. Green, Rhonda M. Morgan, Catherine M. Ohara, and David C. Redding, "Andaptive cross-correlation algorithm for extended scene Shack-Hartmann wavefront sensing," submitted to *Optics Letters* (2007).
8. R. M. Morgan, K. ShCheglov, J. J. Green, C. M. Ohara, J. Roberts, and E. Sidick, "Testbed for extended-scene Shack-Hartmann and phase retrival wavefront sensing," *Proc. SPIE* **5903**, pp.590301 (2005).
9. Joseph J. Green and Bobby R. Hunt, "Improved restoration of space object imagery," J. Opt. Soc. Am. A 16, 2859-2865 (1999).

This paper is a continuation of the previously published papers by Erkin Sidick with the following Clearance Numbers:

1. CL#07-0446 (SRS 2007, OSA, paper for the Conference Proceedings, 29 Jan. 2007)
2. CL#07-0712 (SPIE 2007 Conference Abstract, 26 Feb. 2007)
3. CL#07-1782 (SRS 2007, OSA, conference presentation, 7 June 2007)

Erkin Sidick
Tel: 818-393-7585